SCIENTIFIC REP⚙RTS

OPEN

In–situ XRD and EDS method study on the oxidation behaviour of Ni–Cu sulphide ore

Guangshi Li, Hongwei Cheng, Xiaolu Xiong, Xionggang Lu, Cong Xu, Changyuan Lu, Xingli Zou & Qian Xu

The oxidation mechanism of sulfides is the key issue during the sulphide–metallurgy process. In this study, the phase transformation and element migration were clearly demonstrated by in–situ laboratory–based X–ray diffraction (XRD) and energy–dispersive X–ray spectroscopy (EDS), respectively. The reaction sequence and a four–step oxidation mechanism were proposed and identified. The elemental distribution demonstrated that at a low temperature, the Fe atoms diffused outward and the Ni/Cu atoms migrated toward the inner core, whereas the opposite diffusion processes were observed at a higher temperature. Importantly, the unique visual presentation of the oxidation behaviour provided by the combination of in–situ XRD and EDS might be useful for optimising the process parameters to improve the Ni/Cu extraction efficiency during Ni–Cu sulphide metallurgy.

Since the first super–large magmatic Ni–Cu–platinum–group elements (PGE) deposit (Sudbury, Canada) was discovered in 1883, several super–large Ni–Cu–PGE deposits rich in sulphides have been mined (e.g., Jinchuan Ni–Cu–Co–PGE deposit (China), Noril'sk Ni–Cu–PGE and Pechenga Ni–Cu–PGE deposits (Russia), Voisey's Bay Ni–Cu–Co deposit (Canada))[1]. Magmatic–sulphide deposits host ~40% of the global Ni resources and supply ~60% of the Ni in the world market. With the unceasing mining and consumption of the rich ore resources, the extensive exploitation and utilization of low–grade nickel sulphide ores are becoming important problems for the sustainability of nickel production.

As a traditional pyrometallurgy method, the flash smelting–converter–grinding–floatation–anode electrolysis process requires a high nickel concentrate and is tedious and complicated. From the 1960s to the 1990s, an oxidation–sulphation roasting process followed by leaching was proposed and investigated to treat low–grade Ni–Cu sulphide ores[2–6]. The oxidation behaviour of sulphide ores, which is of principal and vital importance in the sulphide–extraction metallurgy process, is complex and highly dependent on the sulphides phases in the minerals. Pentlandite (expressed as Pn) and chalcopyrite (expressed as Ccp), which are the common minerals used in pyrometallurgical nickel and copper production, respectively, have been theoretically and experimentally investigated during the oxidative–roasting process by many researchers for decades[7–16]. A detailed review of the oxidation mechanisms of Pn and Ccp is presented in Fig. 1.

Early on, the various oxidative reactions of natural Pn were deduced and summarised via thermogravimetric (TG)/mass spectroscopy (MS) analysis, differential thermal analysis (DTA), and X–ray diffraction (XRD) analysis by Dunn et al.[8]. Recently, researchers studied the isothermal oxidation behaviour of synthetic Pn in depth and proposed a novel stepwise phase–transformation mechanism[13, 14]. As shown in Fig. 1, pure Pn is first decomposed into intermediate sulphide (e.g., $(Fe,Ni)_xS_y$, $Fe_yNi_{1-y}S$, Ni_3S_2, NiS) and finally oxidised into Fe_2O_3, NiO, and $Ni_xFe_{2+x}O_4$. For the past few years, researchers have tended to investigate the oxidation behaviour of Pn taken nickel concentrate as a raw material[15, 17–19].

As the most exploited mineral for the extraction metallurgy of copper, Ccp has been extensively studied theoretically and experimentally[7, 9–12, 16, 20–23]. Prasad et al.[17] suggested that it was extremely important and necessary for copper extraction to concentrate on the oxidative–roasting procedure of Ccp. Various reactions occurring in the oxidation of Ccp were summarised in early studies and are briefly presented in Fig. 1[7, 13–15, 17, 18, 21, 22, 24, 25]. As shown in this figure, the first stage is the oxidation of Ccp into Cu_2S (or Cu_5FeS_4) and FeS. This is followed by the formation of metal sulphates and finally the decomposition of the sulphates of iron and copper into oxides (e.g.,

State Key Laboratory of Advanced Special Steel & School of Materials Science and Engineering, Shanghai University, No. 149 Yanchang Road, Shanghai, 200072, China. Correspondence and requests for materials should be addressed to H.C. (email: hwcheng@shu.edu.cn) or X.L. (email: luxg@shu.edu.cn)
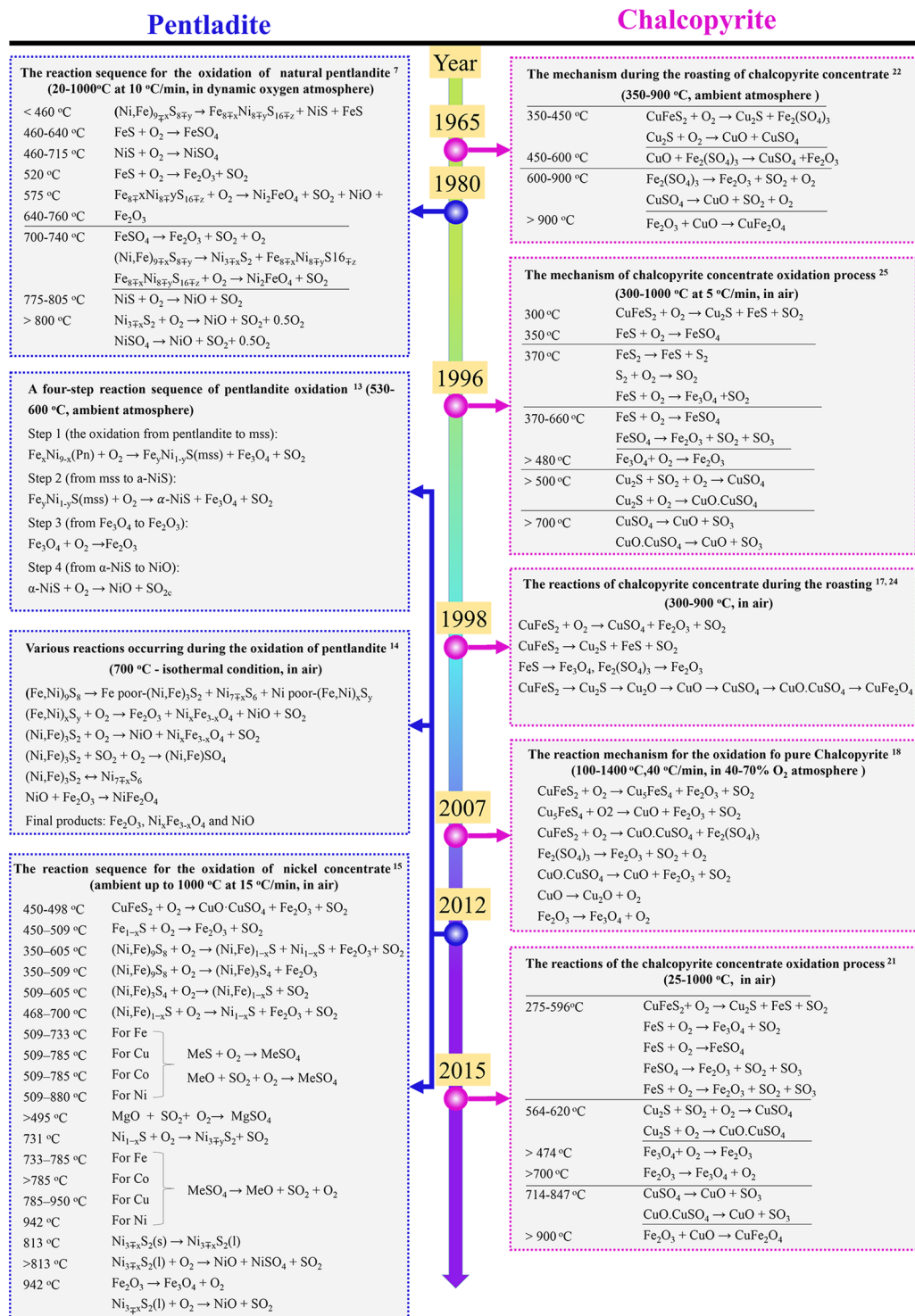
Pentladite   Year   **Chalcopyrite**

The reaction sequence for the oxidation of natural pentlandite [7]
(20–1000°C at 10 °C/min, in dynamic oxygen atmosphere)

< 460 °C	$(Ni,Fe)_{9\mp x}S_{8\mp y} \rightarrow Fe_{8\mp x}Ni_{8\mp y}S_{16\mp z} + NiS + FeS$
460–640 °C	$FeS + O_2 \rightarrow FeSO_4$
460–715 °C	$NiS + O_2 \rightarrow NiSO_4$
520 °C	$FeS + O_2 \rightarrow Fe_2O_3 + SO_2$
575 °C	$Fe_{8\mp x}Ni_{8\mp y}S_{16\mp z} + O_2 \rightarrow Ni_2FeO_4 + SO_2 + NiO + Fe_2O_3$
640–760 °C	
700–740 °C	$FeSO_4 \rightarrow Fe_2O_3 + SO_2 + O_2$
	$(Ni,Fe)_{9\mp x}S_{8\mp y} \rightarrow Ni_{3\mp x}S_2 + Fe_{8\mp x}Ni_{8\mp y}S16_{\mp z}$
	$Fe_{8\mp x}Ni_{8\mp y}S_{16\mp z} + O_2 \rightarrow Ni_2FeO_4 + SO_2$
775–805 °C	$NiS + O_2 \rightarrow NiO + SO_2$
> 800 °C	$Ni_{3\mp x}S_2 + O_2 \rightarrow NiO + SO_2 + 0.5O_2$
	$NiSO_4 \rightarrow NiO + SO_2 + 0.5O_2$

A four-step reaction sequence of pentlandite oxidation [13] (530–600 °C, ambient atmosphere)

Step 1 (the oxidation from pentlandite to mss):
$Fe_xNi_{9-x}(Pn) + O_2 \rightarrow Fe_yNi_{1-y}S(mss) + Fe_3O_4 + SO_2$

Step 2 (from mss to a-NiS):
$Fe_yNi_{1-y}S(mss) + O_2 \rightarrow \alpha\text{-}NiS + Fe_3O_4 + SO_2$

Step 3 (from Fe_3O_4 to Fe_2O_3):
$Fe_3O_4 + O_2 \rightarrow Fe_2O_3$

Step 4 (from α-NiS to NiO):
$\alpha\text{-}NiS + O_2 \rightarrow NiO + SO_{2c}$

Various reactions occurring during the oxidation of pentlandite [14]
(700 °C – isothermal condition, in air)

$(Fe,Ni)_9S_8 \rightarrow Fe\text{ poor-}(Ni,Fe)_3S_2 + Ni_{7\mp x}S_6 + Ni\text{ poor-}(Fe,Ni)_xS_y$
$(Fe,Ni)_xS_y + O_2 \rightarrow Fe_2O_3 + Ni_xFe_{3-x}O + NiO + SO_2$
$(Ni,Fe)_3S_2 + O_2 \rightarrow NiO + Ni_xFe_{3-x}O_4 + SO_2$
$(Ni,Fe)_3S_2 + SO_2 + O_2 \rightarrow (Ni,Fe)SO_4$
$(Ni,Fe)_3S_2 \leftrightarrow Ni_{7\mp x}S_6$
$NiO + Fe_2O_3 \rightarrow NiFe_2O_4$
Final products: Fe_2O_3, $Ni_xFe_{3-x}O_4$ and NiO

The reaction sequence for the oxidation of nickel concentrate [15]
(ambient up to 1000 °C at 15 °C/min, in air)

450–498 °C	$CuFeS_2 + O_2 \rightarrow CuO \cdot CuSO_4 + Fe_2O_3 + SO_2$
450–509 °C	$Fe_{1\rightarrow x}S + O_2 \rightarrow Fe_2O_3 + SO_2$
350–605 °C	$(Ni,Fe)_9S_8 + O_2 \rightarrow (Ni,Fe)_{1\rightarrow x}S + Ni_{1\rightarrow x}S + Fe_2O_3 + SO_2$
350–509 °C	$(Ni,Fe)_9S_8 + O_2 \rightarrow (Ni,Fe)_3S_4 + Fe_2O_3$
509–605 °C	$(Ni,Fe)_3S_4 + O_2 \rightarrow (Ni,Fe)_{1\rightarrow x}S + SO_2$
468–700 °C	$(Ni,Fe)_{1\rightarrow x}S + O_2 \rightarrow Ni_{1-x}S + Fe_2O_3 + SO_2$
509–733 °C	For Fe
509–785 °C	For Cu $MeS + O_2 \rightarrow MeSO_4$
509–785 °C	For Co
509–880 °C	For Ni
>495 °C	$MgO + SO_2 + O_2 \rightarrow MgSO_4$
731 °C	$Ni_{1\rightarrow x}S + O_2 \rightarrow Ni_{3\mp y}S_2 + SO_2$
733–785 °C	For Fe
>785 °C	For Co $MeSO_4 \rightarrow MeO + SO_2 + O_2$
785–950 °C	For Cu
942 °C	For Ni
813 °C	$Ni_{3\mp x}S_2(s) \rightarrow Ni_{3\mp x}S_2(l)$
>813 °C	$Ni_{3\mp x}S_2(l) + O_2 \rightarrow NiO + NiSO_4 + SO_2$
942 °C	$Fe_2O_3 \rightarrow Fe_3O_4 + O_2$
	$Ni_{3\mp x}S_2(l) + O_2 \rightarrow NiO + SO_2$

Year timeline: 1965, 1980, 1996, 1998, 2007, 2012, 2015

The mechanism during the roasting of chalcopyrite concentrate [22]
(350–900 °C, ambient atmosphere)

350–450 °C	$CuFeS_2 + O_2 \rightarrow Cu_2S + Fe_2(SO_4)_3$
	$Cu_2S + O_2 \rightarrow CuO + CuSO_4$
450–600 °C	$CuO + Fe_2(SO_4)_3 \rightarrow CuSO_4 + Fe_2O_3$
600–900 °C	$Fe_2(SO_4)_3 \rightarrow Fe_2O_3 + SO_2 + O_2$
	$CuSO_4 \rightarrow CuO + SO_2 + O_2$
> 900 °C	$Fe_2O_3 + CuO \rightarrow CuFe_2O_4$

The mechanism of chalcopyrite concentrate oxidation process [25]
(300–1000 °C at 5 °C/min, in air)

300 °C	$CuFeS_2 + O_2 \rightarrow Cu_2S + FeS + SO_2$
350 °C	$FeS + O_2 \rightarrow FeSO_4$
370 °C	$FeS_2 \rightarrow FeS + S_2$
	$S_2 + O_2 \rightarrow SO_2$
	$FeS + O_2 \rightarrow Fe_3O_4 + SO_2$
370–660 °C	$FeS + O_2 \rightarrow FeSO_4$
	$FeSO_4 \rightarrow Fe_2O_3 + SO_2 + SO_3$
> 480 °C	$Fe_3O_4 + O_2 \rightarrow Fe_2O_3$
> 500 °C	$Cu_2S + O_2 \rightarrow CuSO_4$
	$Cu_2S + O_2 \rightarrow CuO \cdot CuSO_4$
> 700 °C	$CuSO_4 \rightarrow CuO + SO_3$
	$CuO \cdot CuSO_4 \rightarrow CuO + SO_3$

The reactions of chalcopyrite concentrate during the roasting [17, 24]
(300–900 °C, in air)

$CuFeS_2 + O_2 \rightarrow CuSO_4 + Fe_2O_3 + SO_2$
$CuFeS_2 \rightarrow Cu_2S + FeS + SO_2$
$FeS \rightarrow Fe_3O_4, Fe_2(SO_4)_3 \rightarrow Fe_2O_3$
$CuFeS_2 \rightarrow Cu_2S \rightarrow Cu_2O \rightarrow CuO \rightarrow CuSO_4 \rightarrow CuO \cdot CuSO_4 \rightarrow CuFe_2O_4$

The reaction mechanism for the oxidation fo pure Chalcopyrite [18]
(100–1400 °C, 40 °C/min, in 40–70% O_2 atmosphere)

$CuFeS_2 + O_2 \rightarrow Cu_5FeS_4 + Fe_2O_3 + SO_2$
$Cu_5FeS_4 + O2 \rightarrow CuO + Fe_2O_3 + SO_2$
$CuFeS_2 + O_2 \rightarrow CuO \cdot CuSO_4 + Fe_2(SO_4)_3$
$Fe_2(SO_4)_3 \rightarrow Fe_2O_3 + SO_2 + O_2$
$CuO \cdot CuSO_4 \rightarrow CuO + Fe_2O_3 + SO_2$
$CuO \rightarrow Cu_2O + O_2$
$Fe_2O_3 \rightarrow Fe_3O_4 + O_2$

The reactions of the chalcopyrite concentrate oxidation process [21]
(25–1000 °C, in air)

275–596°C	$CuFeS_2 + O_2 \rightarrow Cu_2S + FeS + SO_2$
	$FeS + O_2 \rightarrow Fe_3O_4 + SO_2$
	$FeS + O_2 \rightarrow FeSO_4$
	$FeSO_4 \rightarrow Fe_2O_3 + SO_2 + SO_3$
	$FeS + O_2 \rightarrow Fe_2O_3 + SO_2 + SO_3$
564–620 °C	$Cu_2S + SO_2 + O_2 \rightarrow CuSO_4$
	$Cu_2S + O_2 \rightarrow CuO \cdot CuSO_4$
> 474 °C	$Fe_3O_4 + O_2 \rightarrow Fe_2O_3$
>700 °C	$Fe_2O_3 \rightarrow Fe_3O_4 + O_2$
714–847 °C	$CuSO_4 \rightarrow CuO + SO_3$
	$CuO \cdot CuSO_4 \rightarrow CuO + SO_3$
> 900 °C	$Fe_2O_3 + CuO \rightarrow CuFe_2O_4$

Figure 1. Summary of the oxidative reaction sequence for Pn and Ccp from early research.

CuO.CuSO$_4$, CuO, Fe$_2$O$_3$, Cu$_x$Fe$_{3-x}$O$_{4-y}$). A. Baba *et al.*[23] conducted a detailed review of the role of Ccp in the pyrometallurgical and hydrometallurgical processes of copper, and suggested that low–grade complex sulphide ores have attracted attention because of the recent decline in deposits of high–grade ores.

Another interesting and important problem that occurs during the oxidative roasting of polymetallic sulphides is the elemental distribution of the ore grains. Many researchers[13–15, 17, 21, 22, 26] have investigated the preferential oxidation of Fe and S during the roasting process using energy–dispersive X–ray spectroscopy (EDS), reporting that the Ni or Cu tends to diffuse into the centre while Fe migrates outward to the oxide rim layer.

Given the aforementioned findings, the oxidation mechanism of the sulphide mineral, which is a long– and well–studied problem, has been investigated in detail using traditional analysis and characterization methods,
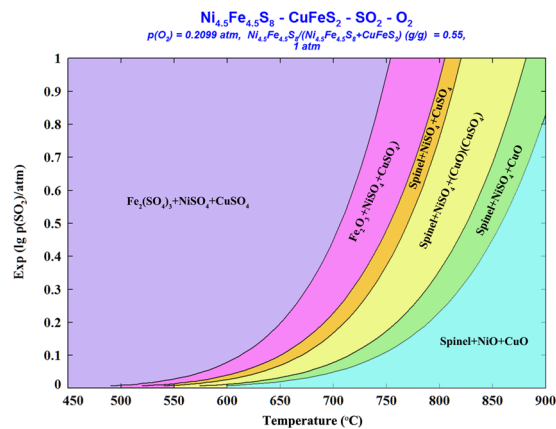
Figure 2. Predominance area diagram for the $Ni_{4.5}Fe_{4.5}S_8$–$CuFeS_2$–SO_2–O_2 system in the temperature range of 450 to 900 °C in air (p(O_2) = 0.21 atm).
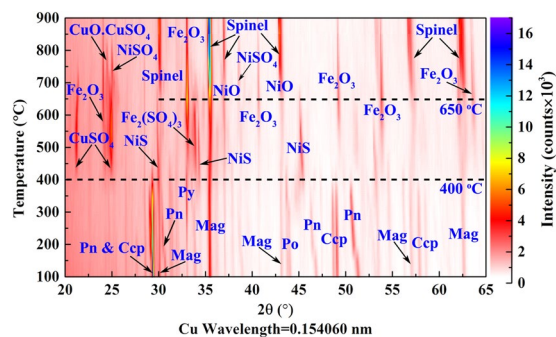

Figure 3. In–situ laboratory–based XRD data collected for the Ni–Cu sulphide ore sample at different temperatures (every 50 °C from 100 to 900 °C, with a heating rate of 5 °C/min) under the isothermal condition during the oxidative–roasting process.

such as TG, DTA, MS, XRD and EDS. Because of the complexity of the Ni–Cu sulphide ore and the weakness of traditional characterization methods, some of the oxidation mechanisms proposed by early researchers should be further examined. However, thorough studies on the oxidative mechanism of polymetallic sulphide minerals have rarely been reported. The in–situ XRD method, which has recently been used to investigate the mechanism of the metallurgical process, is growing in popularity[27–34]. In this study, the oxidation behaviour of a Ni–Cu sulphide ore was investigated in detail during the roasting process using in–situ laboratory–based XRD and EDS in tandem.

Results and Discussion

Phase evolution during oxidation process. To investigate the thermodynamics of the Ni–Cu sulphide mineral system, a phase–stability diagram for the $Ni_{4.5}Fe_{4.5}S_8$–$CuFeS_2$–SO_2–O_2 system at 450 to 900 °C in air (p(O_2) = 0.21 atm) was developed using the Factsage software package[35]. As shown in Fig. 2, at the lower temperatures, the main stable phases were metal sulphates ($Fe_2(SO_4)_3$, $CuSO_4$, and $NiSO_4$) together with Fe_2O_3. As the temperature increases, the predominance areas shift toward the formation of oxides.

The TG and differential TG (DTG) curves for different heating rates in Fig. S2a and b are similar in shape, and the peaks shift to a higher temperature as the heating rate increases. The TG cures in Fig. S2a indicate that there was a gradual mass increase in the range of 400 to 550 °C and that the mass tended to decrease around 550 °C. Correspondingly, Fig. S2b shows that the formation of metal sulphates might be responsible for the two peaks (peak 1 and 2) that occurred during the mass–increasing process, whereas the other four peaks (peaks 3, 4, 5, and 6) might result from the direct oxidation of sulphides into oxides and the decomposition of the formed sulphates. Fig. S2c shows that the amount of sulphates increased at different rates as the temperature increased; reached maximums of approximately 550, 600, and 700 °C for $Fe_2(SO_4)_3$, $CuSO_4$, and $NiSO_4$, respectively; and finally decomposed at higher temperatures.

In–situ laboratory–based XRD analysis was performed to explore the phase transformation of the Ni–Cu sulphide ore during the oxidative–roasting process. Fig. 3 plots the accumulated in–situ XRD data collected during the roasting process. And weight fractions of the phases present at each temperature are shown in Fig. S3. At "low" temperatures (here defined as <300 °C), the peak intensity of the sulphides (Pn, Ccp, and pyrrhotite (Fe$_7$S$_8$)) slowly decreased, but as the temperature increased, the peak intensity of pyrite (FeS_2) increased, which indicates that Pn, Ccp, and pyrrhotite slowly decomposed[36]. When the temperature reached 350 °C or higher, the sulphides oxidised rapidly and disappeared round 400, 450 and 500 °C for Pn, Pyrrhotite and Ccp respectively,
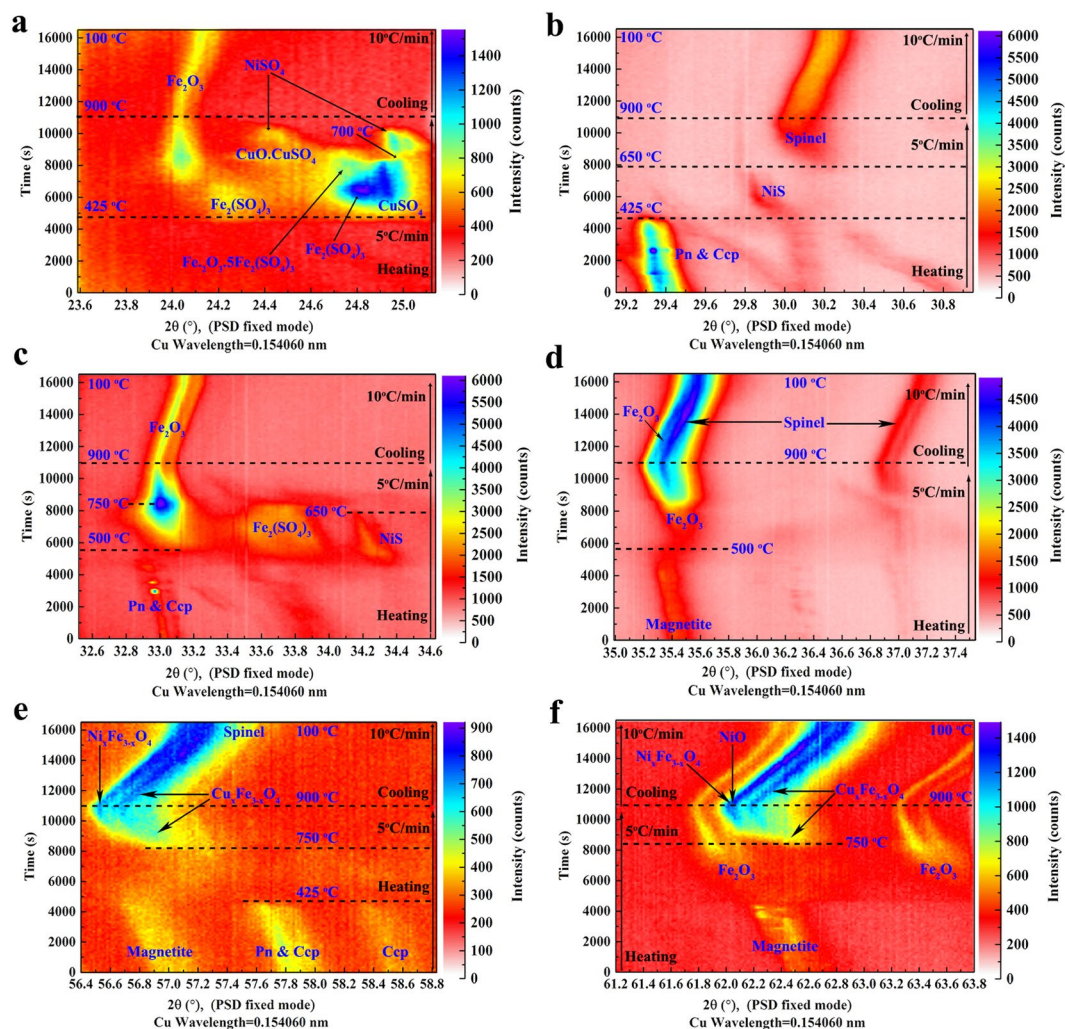
Figure 4. Series of characteristic peaks (2θ angle approximately 21°, 28°, 32°, 35°, 56°, and 61° for (**a–f** respectively) obtained with a small angle range (~2° in 2θ) using in–situ laboratory–based XRD with the PSD fixed model during the oxidative–roasting process.

and the initial oxidative products were metal sulphates ($Fe_2(SO_4)_3$, $CuSO_4$) and NiS. In the range of 350 to 650 °C, the peak intensity of Fe_2O_3 gradually increased, reaching its maximum at 650 °C. As the temperature increased from 500 to 700 °C, the NiS phase gradually decreased and was eventually eliminated; however, the spinel and NiO phases exhibited a different behaviour. As the temperature increased from 650 to 900 °C, the spinel and NiO phases increased, while the Fe_2O_3 phase tended to decrease. As shown in Figs 3 and S3, the generation and trans-formation processes differed significantly among the sulphate phases. For example, the $Fe_2(SO_4)_3$ phase appeared at 400 °C and disappeared at ~650 °C (Fig. S3c); however, the appearance and increase of the $NiSO_4$ phase occurred at 550–700 °C, and the $NiSO_4$ decomposed and disappeared at 850 °C (Fig. S3a). The $CuSO_4$ phase was generated together with the $Fe_2(SO_4)_3$ phase at 400 °C and then gradually disappeared with the appearance and increase of the $CuO.CuSO_4$ phase at 700–800 °C. Finally, the $CuO.CuSO_4$ phase disappeared at 850 °C (Fig. S3b).

For a better understanding of the oxidation behaviour of the Ni–Cu sulphide ore, a series of characteristic–peak ranges were measured using the in–situ laboratory–based XRD with the position–sensitive detector (PSD) fixed model. According to the patterns shown in Fig. 4, the oxidative processes of the Ni–Cu sulphide ore are discussed in detail as follows:

Initial oxidative stage: At the beginning, the sulphide–mineral sample hardly changed as the temperature increased. However, there may have been subtle variations in the peak intensities for Pn and Ccp, as shown in Fig. 4b and c, which indicated the slow decomposition of the sulphides[8]. Then, both the Pn and Ccp disappeared rapidly at ~425 °C, as shown in Fig. 4b,c and e. The Mag was gradually oxidised into Fe_2O_3 above 425 °C, as shown in Fig. 4d,e and f.

Sulphation stage: As shown in Figs 4a,c and S3, the sulphates ($Fe_2(SO_4)_3$ and $CuSO_4$) were formed almost instantaneously around 425 °C and increased gradually with the increase of the oxidation temperature. Figure 4a shows that the $Fe_2(SO_4)_3$ phases gradually transformed into iron oxide (Fe_2O_3) and iron oxide sulphate

($Fe_2O_3 \cdot 5Fe_2(SO_4)_3$) in the temperature range of 500 to 700 °C. Then, the iron oxide sulphate ($Fe_2O_3 \cdot 5Fe_2(SO_4)_3$) decomposed into Fe_2O_3 and disappeared at ~750 °C.

As shown in Fig. 4a, $CuSO_4$ was rapidly generated around 425 °C and remained stable below ~600 °C. CuO. $CuSO_4$, which was detected in the range of 650 to 750 °C, was the decomposition product of $CuSO_4$ (Figure S3b). However, as shown in Fig. 4b and c, the Pn was first transformed into the NiS phase in the temperature range of 425 to 500 °C, and then the NiS phase gradually increased with the temperature, disappearing at ~650 °C. As shown in Fig. 4a, $NiSO_4$ was formed in a higher temperature range—700 to 800 °C—which is consistent with the range shown in Fig. S3a (600 to 800 °C).

Spinel–formation stage: As demonstrated in Fig. 4c, the iron oxide (Fe_2O_3) increased rapidly around 500 °C and reached its maximum value when the temperature increased to ~750 °C. In addition, as shown in Fig. 4a and c, the remarkable changes of the Fe_2O_3 diffraction peak profile occurred during the heating and cooling processes, which might be the results of the growth of Fe_2O_3 crystal. As shown in Fig. S4, the [104] crystal size of Fe_2O_3 firstly increased at the heating stage, remained constant at the temperature range from 600 °C to 700 °C, and increased at temperature up to 800 °C, then remained unchanged until the cooling stage. The spinel phase was initially generated around 750 °C, as shown in Fig. 4b,d,e and f. Then, the spinel phase gradually increased with the temperature. In contrast, the Fe_2O_3 was reduced as the temperature increased. As shown in Fig. 4e and f, the diffraction patterns of the Ni–spinel and Cu–spinel phases were separated and revealed clearly, whereas the diffraction peaks of the NiO and Ni–spinel phases exhibited serious overlap. The Cu–spinel was formed with priority, and then the Ni–spinel and NiO peaks were detected.

Cooling stage: The phase components of the sample remained constant in the cooling stage, as shown in Fig. 4. The diffraction peaks significantly shifted to a large angle because of the lattice contraction during the cooling process. Conversely, the lattice expansion during the roasting caused the peaks to shift to a small angle.

Elemental migration and distribution.

The elemental distribution of the cross–section of the particles was studied by EDS, as discussed in this section. The SEM and EDS analysis of Pn and Ccp grains at different temperatures are shown in Figs S5 and S6, respectively. The element migration in the Pn and Ccp grains was similar in the initial oxidative stage (~450 °C). As shown in Figs 5b and 6b, the Fe atoms in Pn and Ccp migrated to the surface and preferentially oxidised into a dense, thin oxide layer (4–5 μm), whereas the Ni and Cu tended to migrate to the centre of the grains in the earlier oxidation stage. Fig. 5c shows that there were three layers of Pn grains at this stage. According to the in–situ XRD (Figs 3 and 4) and EDS spot (Fig. S5a) analyses, these three layers were the $Fe_2(SO_4)_3$ outer layer, the intermediate thin band of the NiS phase, and the inner core of Pn or $(Ni,Fe)_9S_{8-x}$ (Pn'). However, for the Ccp particles (Fig. 6c and Fig. S6a), the outer side was an Fe_2O_3 dense layer, while the inner side was Ccp or $CuFeS_{2-y}$ (Ccp').

As the temperature increased to 550 °C (Figs 5e, 6e and Figs S5b, S6b), the oxidised gas product (SO_2) diffusing outward collided with the O_2 undergoing inward diffusion at the rim of the Fe_2O_3 layer. As shown in Figs 5f and 6f, the $Fe_2(SO_4)_3$ outer rims were then formed at both the Pn and Ccp grains. Simultaneously, the inward diffusion of O_2 resulted in Ni– and Cu–enriched cores of Pn and Ccp, respectively. The Cu–enriched core further sulphated into $CuSO_4$, whereas the Ni–S enriched core remained stable at 550 °C. This phenomenon is consistent with the sulphate–leaching experiments (Fig. S2a) and the in–situ XRD characterizations (Figs 3 and 4). The aforementioned results suggest that the sulphation of Ccp was preferential over that of Pn. As shown in Figs 5h and 6h, the distribution of S at the outer layer decreased or disappeared, mainly owing to the decomposition of the outer $Fe_2(SO_4)_3$ layers into Fe_2O_3 at 650 °C (Figs S5c and S6c). A clearer and more realistic view of this is provided by comparison with Fig. 5f and i (Fig. 6f and i for Ccp grain).

As shown in Fig. 5k and l, the NiS inner core was oxidised into NiO and $Ni_xFe_{3-x}O_{4-y}$ at 750 °C. There were three layers (NiO–$Ni_xFe_{3-x}O_{4-y}$–Fe_2O_3, from inner to outside) in the Pn grain (Fig. S5d). Surprisingly, however, the sulphation of Ni is not been observed in Fig. 5, possibly because a small amount of $NiSO_4$ formed under this continuous–heating condition and the grains were not selected randomly in this work. For the Ccp grains (Fig. 6k and l), there may have been a $Cu_xFe_{3-x}O_{4-y}$ inner layer with a Fe_2O_3 thin surface after the roasting at 750 °C (Fig. S6d). Another noteworthy phenomenon is that the Ni tended to diffuse outward gradually, as observed by comparing the line–scanning results in Fig. 5h and k (Fig. 5i and l for mapping). Moreover, as shown in Fig. 6k and l, diffuse distributions of Cu, Fe, and O appeared, indicating that the Cu atoms diffused outward more rapidly than the Ni atoms.

Oxidation mechanism of Ni–Cu sulphide ore.

Considering the aforementioned results, the reaction sequence of the Ni–Cu sulphide ore during the roasting in air was deduced, as summarised in Table 1. The oxidation mechanism of Pn and Ccp is proposed as follows and shown in Fig. 7. In the temperature range of 350 to 450 °C, the surface–absorbed O_2 first contacted and reacted with the mineral grains, and a thin Fe_2O_3 layer was formed at this stage. Fe and S were preferentially oxidized over Ni and Cu, which was clearly observed and well–investigated. Consequently, the Fe atoms diffused to the surface, while the Ni and Cu atoms migrated into the inner core. Although many authors have observed and investigated this phenomenon, no reasonable theory has been proposed to explain the internal connection between the preferential oxidation of Fe and the opposite diffusion directions of Fe and Ni (or Cu)[13–15, 17, 18, 22]. Recently, researchers used the ab–initio density functional theory to investigate and explain the preferential oxidation of Fe at the Pn and Ccp surface[37]. And, based on the characterization presented in the present study, this preferential oxidation may have resulted from the chemical–affinity of metals (Fe, Ni and Cu) for oxygen and sulphur[38]. While the Fe was preferentially oxidized into Fe–O phase on the surface of Pn or Ccp crystal structure, the concentration of Fe–S declined sharply, resulting in the outward migration of Fe atoms. Then the Ni/Cu atoms diffused into the inner core and formed Ni–S or Cu–S phase.

As the temperature increased from 450 to 550 °C, Fe and S were continuously preferentially oxidized over Ni and Cu, but the Fe_2O_3 remained at the interlayer between the outer $Fe_2(SO_4)_3$ layer and the inner core (NiS for
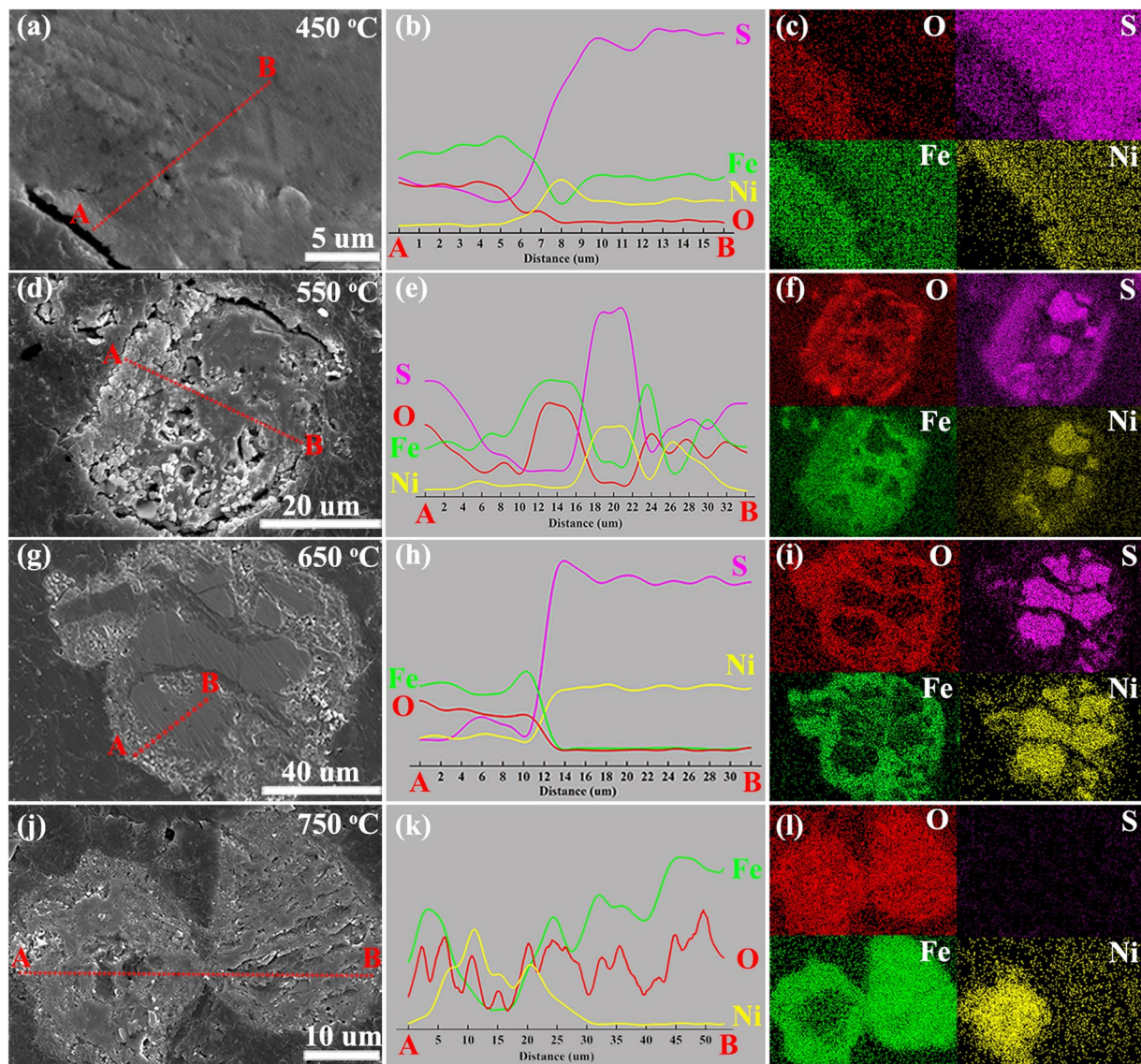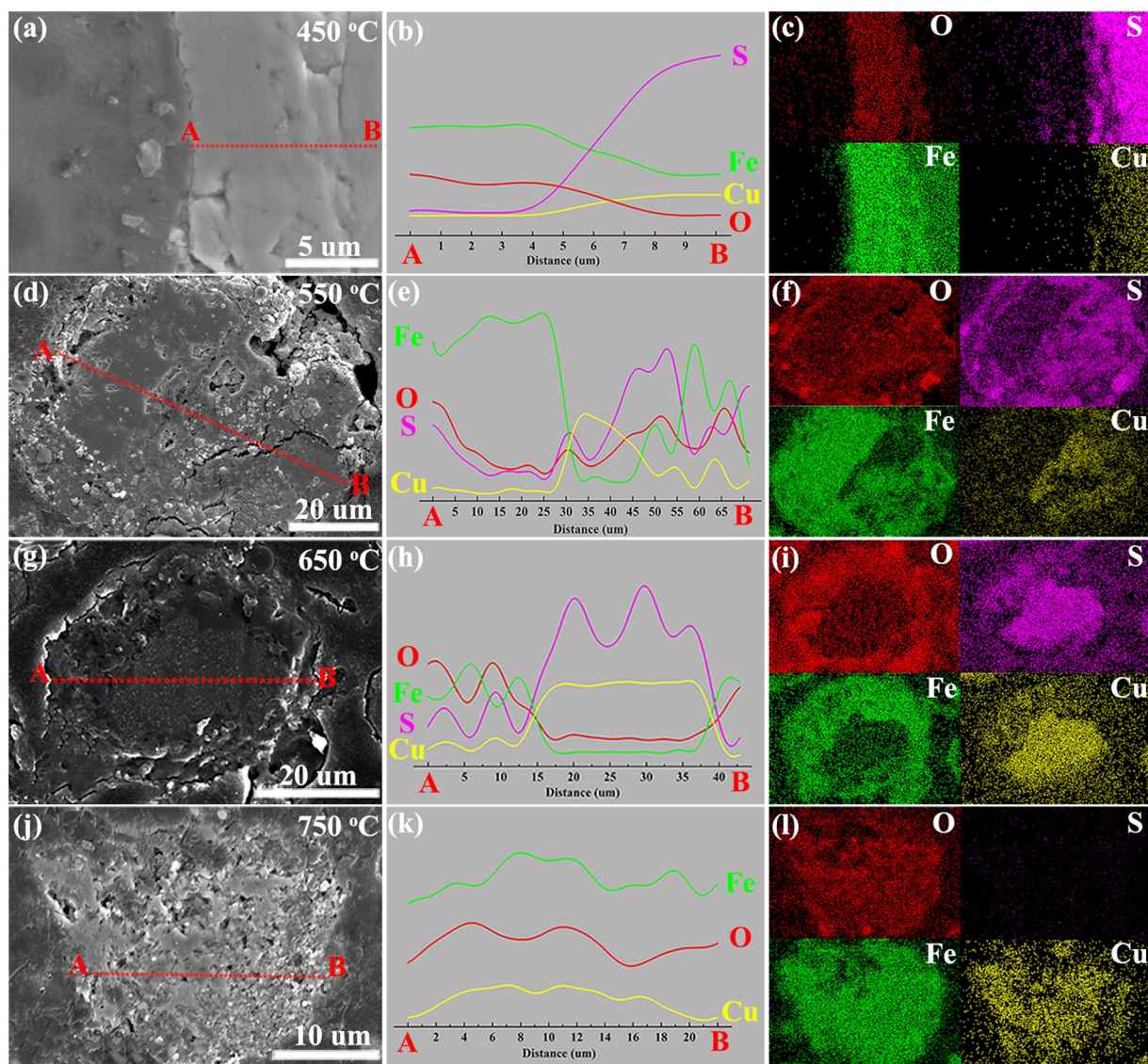
Figure 5. SEM, EDS line–scanning and EDS–mapping results for elements (O, S, Fe, and Ni) over the cross section of Pn particles after the roasting at 450 °C (**a–c**), 550 °C (**d–f**), 650 °C (**g–i**), and 750 °C (**j–l**) in air.

Pn grain, $CuSO_4$ for Ccp grain) at this stage. A large amount of SO_2 gas, which was produced by the oxidation of Fe in the interlayer, diffused outward, possibly reacted with O_2 to form SO_3, and then transformed the previously formed Fe_2O_3 layer into the outer $Fe_2(SO_4)_3$ layer. At this stage, the domain reaction was the sulphation of Fe and Cu, and the NiS in the inner core remained stable.

The sulphation of Ni occurred at a higher temperature (approximately 650–750 °C), and a small amount of $NiSO_4$ was formed at the internal layer between the NiS core and the Fe_2O_3 outer rim at this stage, owing to the small amount of SO_2 concentrate produced by the decomposition of $Fe_2(SO_4)_3$ and $CuSO_4$. A small part of the $CuSO_4$ decomposed and formed a $CuO.CuSO_4$ rim, yet most of the $CuSO_4$ remained stable in the inner core. Hence, this stage was suitable for the sulphation roasting of nickel concentrate, which simultaneously leached Ni and Cu in water and separated Fe from the Ni–Cu sulphide mineral.

The final stage involved the decomposition of $CuO.CuSO_4$, $CuSO_4$, and $NiSO_4$ and the formation of the spinel phase ($M_xFe_{3-x}O_{4-y}$, M = Fe, Co, Ni, Cu, Mg). The Ni and Cu tended to react with the Fe_2O_3 to form a stable spinel phase. The high chemical stability of the spinel phase may lead to the formation of chemical potential at the reactive interface, then may have caused the outward diffusion of Cu/Ni and the inward diffusion of Fe at a higher temperature[39–43]. Moreover, the $Cu_xFe_{3-x}O_{4-y}$ was diffusely distributed in the grain, while the $Ni_xFe_{3-x}O_{4-y}$ was just an internal rim with the inner core of NiO. And it may be due to the difference in cation diffusion rates between Ni and Cu during the roasting process.

In conclusion, the oxidation behaviour of a Ni–Cu sulphide ore, which is closely related to the sulphide–extraction metallurgy process, was thoroughly investigated by in–situ laboratory–based XRD and EDS. A four–step oxidation mechanism, including the preferential oxidation of Fe and S, metal sulphation, the decomposition

Figure 6. SEM, EDS–line–scanning, and EDS–mapping results for elements (O, S, Fe, and Cu) over the cross section of Ccp particles after the roasting at 450 °C (**a–c**), 550 °C (**d–f**), 650 °C (**g–i**), and 750 °C (**j–l**) in air.

of sulphates, and the formation of a spinel phase, was proposed according to phase–diagram analysis, TG–DTG analysis, the sulphate–leaching process, and in–situ XRD patterns. The reaction sequence that occurred during the oxidation of the Ni–Cu sulphide ore was summarised. In addition, the EDS elemental distribution demonstrated that the Fe atoms diffused outward and the Ni/Cu atoms migrated toward the inner core during the first three stages, whereas these diffusion processes were opposite at the final stage, possibly because of chemical–affinity of metals (Fe, Ni and Cu) for oxygen and sulphur and the high chemical stability of the spinel phase, respectively. A unique visual characterization of the oxidation mechanism in the Ni–Cu sulphide ore roasting process was performed by a combination of in–situ XRD and EDS. This mechanism may be conducive to an alternative metallurgy process for the Ni–Cu sulphide ore.

Methods

Sample preparation.   A Ni–Cu sulphide ore sample, which was a product of flotation and originated from Jinchuan Group Ltd., China, was investigated. The powder sample was dried at 100 °C for 24 h and passed over vibrating sieves to obtain an extremely fine powder with a diameter of less than 74 um. XRD analysis indicated that the sample was composed of Pn, magnetite, Ccp, pyrrhotite, lizardite, pyrite, and quartz. XRD quantitative phase analysis (QPA) was performed using the Rietveld refinement method with the TOPAS software[44–47]. The Rietveld refinement of the diffraction pattern resulted in good–quality fits with a goodness of fit (Gof) of nearly 2, as shown in Fig. S1. The results of the XRD quantitative phase analysis of the Ni–Cu sulphide ore sample are presented in Table 2. As shown in Table 3, the content of the major metallic elements (Fe, Ni, Cu) in the sample was determined by X–ray fluorescence (XRF), inductively coupled plasma atomic emission spectroscopy (ICP–AES, for short), and XRD analyses.
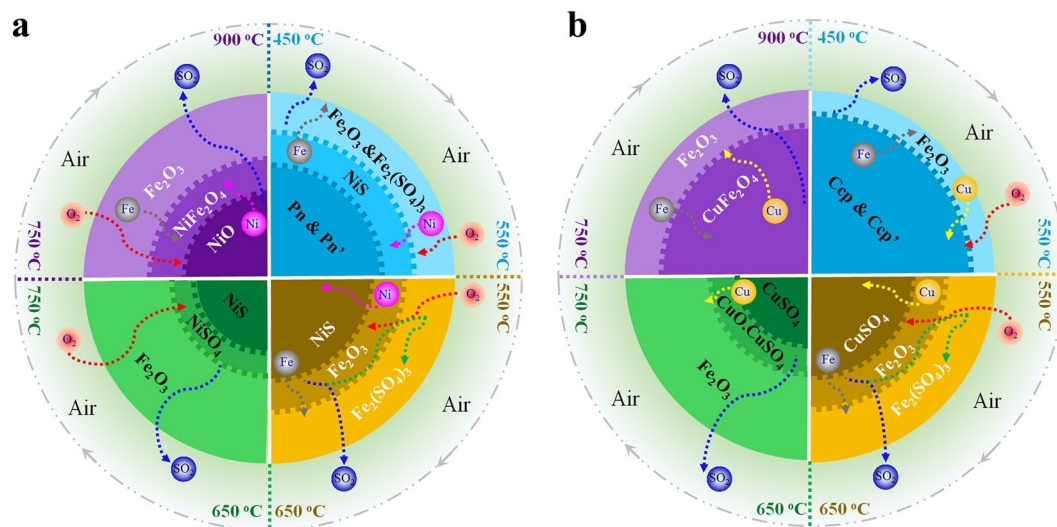
Figure 7. Schematic of the oxidative–roasting mechanisms of Pn (**a**) and Ccp (**b**) in the Ni–Cu sulphide ore. Four temperature ranges were defined, and a four–stage reaction sequence occurred.

350–425 °C	$(Ni,Fe)_9S_8 \, (Pn) \rightarrow (Ni,Fe)_{9-y}S_{8-x} \, (Pn') + FeS + NiS$
	$CuFeS_2 \, (Ccp) \rightarrow CuFe_{1-a}S_{2-x} \, (Ccp') + xFeS$
	$Fe_7S_8 \, (Pyrrhotite) \rightarrow 6FeS + FeS_2$
425–500 °C	$Pn' + O_2 \rightarrow NiS + Fe_2(SO_4)_3$
	$2FeS_2 + 7O_2 \rightarrow Fe_2(SO_4)_3 + SO_2$
	$4Fe_3O_4 \, (Magnetite) + O_2 \rightarrow 6Fe_2O_3$
	$2Fe_3O_4 + 9SO_2 + 5O_2 \rightarrow 3Fe_2(SO_4)_3$
425–650 °C	$2CuFeS_{2-y} \, (Ccp') + (9\text{-}2y)O_2 + (1+2y)SO_2 \rightarrow 2CuSO_4 + Fe_2(SO_4)_3$
500–650 °C	$2NiS + 3O_2 \rightarrow 2NiO + 2SO_2$
	$6Fe_2(SO_4)_3 \rightarrow Fe_2O_3 . 5Fe_2(SO_4)_3 + 3SO_3 \rightarrow 6Fe_2O_3 + 12SO_2$
650–750 °C	$NiS + 2O_2 \rightarrow NiSO_4$
	$2NiO + 2SO_2 + O_2 \rightarrow 2NiSO_4$
650–800 °C	$2CuSO_4 \rightarrow CuO.CuSO_4 + SO_3$
750–900 °C	$NiSO_4 + Fe_2O_3 \rightarrow NiFe_2O_4 + SO_3$
	$NiO + Fe_2O_3 \rightarrow NiFe_2O_4$
	$CuO. CuSO_4 + 2Fe_2O_3 \rightarrow 2CuFe_2O_4 + SO_3$

Table 1. Summary of the reaction sequence that occurred during the oxidative roasting of Ni–Cu sulphide in air.

Mineral	Pentlandite	Magnetite	Chalcopyrite	Pyrrhotite	Lizardite	Pyrite	Quartz
wt%	27.3	23.5	22.8	14.4	4.0	5.1	2.7
Errors%	1.7	1.8	1.5	0.9	0.5	0.5	0.4

Table 2. XRD quantitative phase analysis of the Ni–Cu sulphide ore sample.

Fe			Ni			Cu		
XRF	ICP	XRD	XRF	ICP	XRD	XRF	ICP	XRD
28.3%	34.2%	44.8%	7.7%	9.4%	8.3%	6.5%	6.6%	7.9%

Table 3. Content of the major metallic elements (Fe, Ni, Cu) in Ni–Cu sulphide ore sample, determined by XRF, ICP, and XRD.

TG analysis and oxidative roasting–water leaching experiments. TG analysis was performed to evaluate the oxidation behaviour of Ni–Cu sulphide ore powder samples using a TG analyser (NETZSCH STA

449 F3 Jupiter) at different heating rates (5, 10, and 20 °C/min) in air. 2 g of the Ni–Cu sulphide ore powder sample was put into a crucible (30 mm × 70 mm) and then the crucible was placed in a muffle furnace, which was heated to a target temperature (from 100 to 900 °C in intervals of 50 °C) at a rate of 5 °C/min and maintained for 30 min. The calcines were then leached in 150 mL of water at 80 °C for 2 h to evaluate the amount of sulphate species formed during the oxidative–roasting process. After filtration, the filtrate was analysed by ICP–AES.

In–situ XRD (full–pattern scanning and PSD fixed model).

In–situ laboratory–based XRD experiments were performed using a laboratory X–ray powder diffractometer (Bruker D8 ADVANCE, with Cu Kα1 radiation). An Anton Paar XRK 900 reactor chamber with a Macor sample holder, which was designed for the in–situ XRD investigation of solid–state and solid–gas reactions at temperatures ranging from 25 to 900 °C, was fitted to the diffractometer. The powder sample rested upon a ceramic sieve (pore size of 0.2 mm), so that reactive gas could penetrate the sample and sample holder. XRK 900 was connected to a TCU 750 temperature–control unit. The heating procedure and measuring parameters were set using the control software of the X–ray diffractometer. The in–situ XRD experiments focused on the oxidative–roasting process of the Ni–Cu sulphide ore sample under a 40 mL/min flow of air steam.

For the full–pattern scanning model of the in–situ XRD, the sample was heated from 25 to 900 °C at 5 °C/min. XRD patterns were collected at different temperatures (every 50 °C from 100 to 900 °C°C) under the isothermal condition. To ensure that the reactions approach chemical equilibrium, a delay of 30 min was set for the data collections. The patterns were recorded in the 2θ range of 20 to 65° with a step size of 0.02° and a counting time of 1 s per step. The diffraction patterns were analysed by Rietveld refinement using TOPAS software[44–47], allowing phase abundances to be quantified.

For the PSD fixed model of the in–situ XRD, the detector was set at a fixed angle to enable the simultaneous detection of a certain 2θ range of the diffraction–pattern data. The sample was roasted from 25 to 900 °C at 5 °C/min and cooled to room temperature at −10 °C/min. A certain 2θ angle (approximately 21°, 28°, 32°, 35°, 56°, and 61°) was set as the starting angle to collect the characteristic diffraction–pattern data instantaneously throughout the heating and cooling process. The opening slit of the detector was set as 2.8° (the maximum value), allowing us to obtain diffraction patterns over the maximum 2θ range. The diffraction data were collected with a counting time of 2 min for each point, yielding temperature resolutions of 10 and 20 °C during the heating and cooling, respectively.

EDS characterization of oxidative–roasting samples.

The Ni–Cu sulphide ore sample was evenly sprinkled on four corundum crucibles, forming ultrathin layers of mineral particles at the bottom of each crucible. The four resulting samples were roasted in a muffle furnace in the ambient atmosphere from 25 °C to 450, 550, 650, and 750 °C, respectively, at a heating rate of 5 °C/min. When the given temperature was reached, the samples were removed from the furnace and immediately quenched in liquid nitrogen. The cooling oxidative–powder samples were mounted in epoxy resin. Then, the cured epoxy samples were ground with metallographic abrasive paper and polished on a diamond pad with an oil–based 0.3–μm diamond suspension as the polishing media. Finally, the polished samples were coated with Pt and then characterised using a scanning electron microscope (SU–1500, Hitachi) complemented by an energy–dispersive X–ray detector (Oxford Inca X–Max).

References

1. Song, X., Wang, Y. & Chen, L. Magmatic Ni–Cu–(PGE) deposits in magma plumbing systems: Features, formation and exploration. *Geoscience Frontiers.* **2**, 375–384, doi:10.1016/j.gsf.2011.05.005 (2011).
2. Thornhill, P. G. Method of roasting metal sulfide concentrates in a fluidized bed. U.S. patent 2,813,015 (1957).
3. Thornhill, P. G. Method of roasting metal sulfide concentrates in a fluidized bed. U.S. patent 2,813,016 (1957).
4. Thornhill, P. G. Fluidized bed roasting of metal sulfide concentrates. U.S. patent 2,930,604 (1960).
5. Frankiewicz, T. C. Selective sulfation process for partitioning ferrous and non–ferrous values in an ore. U.S. patent 4,110,106 (1978).
6. Saikkonen, P. J. Process for recovering non–ferrous metal values from ores, concentrates, oxidic roasting products or slags. U.S. patent 4,464,344 (1984).
7. Dunn, J. G. The oxidation of sulphide minerals. *Thermochimica Acta.* **300**, 127–139, doi:10.1016/S0040-6031(96)03132-2 (1997).
8. Pandher, R. & Utigard, T. Roasting of nickel concentrates. *Metallurgical and Materials Transactions B.* **41**, 780–789, doi:10.1007/s11663-010-9373-5 (2010).
9. Acres, R. G., Harmer, S. L. & Beattie, D. A. Synchrotron PEEM and ToF–SIMS study of oxidized heterogeneous pentlandite, pyrrhotite and chalcopyrite. *Journal of synchrotron radiation.* **17**, 606–615, doi:10.1107/S0909049510026749 (2010).
10. Pandher, R., Thomas, S., Yu, D., Barati, M. & Utigard, T. Sulfate formation and decomposition of nickel concentrates. *Metallurgical and Materials Transactions B.* **42**, 291–299, doi:10.1007/s11663-010-9466-1 (2011).
11. Yu, D. & Utigard, T. A. TG/DTA study on the oxidation of nickel concentrate. *Thermochimica Acta.* **533**, 56–65, doi:10.1016/j.tca.2012.01.017 (2012).
12. Dunn, J. & Kelly, C. A TG/MS and DTA study of the oxidation of pentlandite. *Journal of Thermal Analysis and Calorimetry.* **18**, 147–154, doi:10.1007/BF01909462 (1980).
13. Xia, F., Pring, A. & Brugger, J. Understanding the mechanism and kinetics of pentlandite oxidation in extractive pyrometallurgy of nickel. *Minerals Engineering.* **27–28**, 11–19, doi:10.1016/j.mineng.2011.12.001 (2012).
14. Zhu, H., Chen, J., Deng, J., Yu, R. & Xing, X. Oxidation behavior and mechanism of pentlandite at 973 K (700 °C) in air. *Metallurgical and Materials Transactions B.* **43**, 494–502, doi:10.1007/s11663-011-9630-2 (2012).
15. Yu, D., Utigard, T. A. & Barati, M. Fluidized bed selective oxidation–sulfation roasting of Nickel sulfide concentrate: part I. oxidation roasting. *Metallurgical and Materials Transactions B.* **45**, 653–661, doi:10.1007/s11663-013-9958-x (2014).
16. Tsukada, H., Asaki, Z., Tanabe, T. & Kondo, Y. Oxidation of mixed copper–iron sulfide. *Metallurgical Transactions B.* **12**, 603–609, doi:10.1007/BF02654333 (1981).
17. Prasad, S. & Pandey, B. D. Alternative processes for treatment of chalcopyrite – A review. *Minerals Engineering.* **11**, 763–781, doi:10.1016/S0892-6875(98)00061-2 (1998).
18. Perez–Fontes, S., Perez–Tello, M., Prieto–Lopez, L., Brown, F. & Castillon–Barraza, F. Thermoanalytical study on the oxidation of sulfide minerals at high temperatures. *Minerals and Metallurgical Processing.* **24**, 275–283 (2007).

19. Burger, E., Bourgarit, D., Frotté, V. & Pilon, F. Kinetics of iron–copper sulphides oxidation in relation to protohistoric copper smelting. *Journal of Thermal Analysis and Calorimetry.* **103**, 249–256, doi:10.1007/s10973-010-0926-2 (2010). 2.

20. Savinova, Y. A., Popov, V. A., Portov, A. B. & Tsemekhman, L. S. Roasting of a sulfide polymetallic concentrate in a fluidized bed furnace. *Russian Metallurgy (Metally).* **2014**, 351–357, doi:10.1134/S0036029514050115 (2014).

21. Mitovski, A. *et al.* Thermal analysis and kinetics of the chalcopyrite–pyrite concentrate oxidation process. *Metalurgija.* **54**, 311–314 (2015).

22. Razouk, R. I., Kolta, G. A. & Mikhail, R. S. The roasting of copper sulphides. II. Natural copper sulphides. *Journal of Applied Chemistry.* **15**, 191–196, doi:10.1002/jctb.5010150406 (1965).

23. A. Baba, A. *et al.* A review on novel techniques for chalcopyrite ore processing. *Journal of Mining Engineering and Mineral Processing.* **1**, 1–16, doi:10.5923/j.mining.20120101.01 (2012).

24. Prasad, S. & Pandey, B. D. Thermoanalytical studies on copper—iron sulphides. *Journal of Thermal Analysis and Calorimetry.* **58**, 625–637, doi:10.1023/A:1010108729034 (1999).

25. Živković, Zi. D., Mitevska, N. & Savović, V. Kinetics and mechanism of the chalcopyrite–pyrite concentrate oxidation process. *Thermochimica Acta.* **282–283**, 121–130, doi:10.1016/0040-6031(96)02883-3 (1996).

26. Tanabe, T. *et al.* Oxidation kinetics of dense pentlandite. *Transactions of the Japan Institute of Metals.* **28**, 977–985, doi:10.2320/matertrans1960.28.977 (1987).

27. Madsen, I. C., Scarlett, N. V. Y. & Whittington, B. I. Pressure acid leaching of nickel laterite ores: an in situ diffraction study of the mechanism and rate of reaction. *Journal of Applied Crystallography.* **38**, 927–933, doi:10.1107/S002188980502813X (2005).

28. Bhagat, R. *et al.* In situ synchrotron diffraction of the electrochemical reduction pathway of TiO_2. *Acta Materialia.* **58**, 5057–5062, doi:10.1016/j.actamat.2010.05.041 (2010).

29. Fu, X., Wang, Y. & Wei, F. Phase transitions and reaction mechanism of ilmenite oxidation. *Metallurgical and Materials Transactions A.* **41**, 1338–1348, doi:10.1007/s11661-010-0173-y (2010).

30. Majuste, D., Ciminelli, V. S. T., Eng, P. J. & Osseo–Asare, K. Applications of in situ synchrotron XRD in hydrometallurgy: Literature review and investigation of chalcopyrite dissolution. *Hydrometallurgy.* **131–132**, 54–66, doi:10.1016/j.hydromet.2012.10.001 (2013).

31. Webster, N. A. S. *et al.* An investigation of goethite–seeded $Al(OH)_3$ precipitation using in situ X–ray diffraction and Rietveld–based quantitative phase analysis. *Journal of Applied Crystallography.* **43**, 466–472, doi:10.1107/S0021889810008484 (2010).

32. Webster, N. A. S., Pownceby, M. I. & Madsen, I. C. In situ X–ray diffraction investigation of the formation mechanisms of silico–ferrite of calcium and aluminium–I–type (SFCA–I–type) complex calcium ferrites. *ISIJ International.* **53**, 1334–1340, doi:10.2355/isijinternational.53.1334 (2013).

33. Webster, N. A. S. *et al.* In situ diffraction studies of iron ore sinter bonding phase formation: QPA considerations and pushing the limits of laboratory data collection. *Powder Diffraction.* **29**(suppl.1), S54–S58, doi:10.1017/S088571561400092X (2014).

34. Webster, N. A. S. *et al.* Fundamentals of silico–ferrite of calcium and aluminum (SFCA) and SFCA–I iron ore sinter bonding phase formation: effects of CaO:SiO₂ ratio. *Metallurgical and Materials Transactions B.* **45**, 2097–2105, doi:10.1007/S11663-014-0137-5 (2014).

35. Bale, C. W. *et al.* FactSage thermochemical software and databases. *Calphad.* **26**, 189–228, doi:10.1016/S0364-5916(02)00035-4 (2002).

36. Wang, H. & Salveson, I. A review on the mineral chemistry of the non-stoichiometric iron sulphide, $Fe_{1-x}S (0 \le x \le 0.125)$: polymorphs, phase relations and transitions, electronic and magnetic structures. *Phase Transitions.* **78**, 547–567, doi:10.1080/01411590500185542 (2005).

37. Mkhonto, P. P., Chauke, H. R. & Ngoepe, P. E. Ab initio studies of O_2 adsorption on (110) nickel–rich pentlandite ($Fe_4Ni_5S_8$) mineral surface. *Minerals.* **5**, 665–678, doi:10.3390/min5040516 (2015).

38. Marakushev, A. A. & Bezmen, N. I. Chemical affinity of metals for oxygen and sulfur. *International Geology Review.* **13**, 1781–1794, doi:10.1080/00206817109475642 (1971).

39. Kenfack, F. & Langbein, H. Spinel ferrites of the quaternary system Cu-Ni-Fe-O: Synthesis and characterization. *Journal of Materials Science.* **41**, 3683–3693, doi:10.1007/s10853-006-6263-y (2006).

40. Karpova, T. S., Vasil'ev, V. G., Vladimirova, E. V. & Nosov, A. P. Synthesis of ferrite spinel $NiFe_2O_4$ by thermal hydrolysis and its magnetic properties. *Inorganic Materials: Applied Research.* **3**, 107–112, doi:10.1134/S2075113312020086 (2012).

41. Iliev, M. N. *et al.* Raman studies of cation distribution and thermal stability of epitaxial spinel $NiCo_2O_4$ films. *Journal of Applied Physics.* **114**, 1–5, doi:10.1063/1.4815874 (2013).

42. Balagurov, A. M. *et al. Crystallography Reports. Structural phase transition in $CuFe2O4$ spinel.* **58**, 710–717, doi:10.1134/S1063774513040044 (2013).

43. Liang, X. *et al.* The valence and site occupancy of substituting metals in magnetite spinel structure $Fe_{3-x}M_xO_4$ (M = Cr, Mn, Co and Ni) and their influence on thermal stability: an XANES and TG-DSC investigation. *Solid State Sciences.* **15**, 115–122, doi:10.1016/j.solidstatesciences.2012.10.005 (2013).

44. Rietveld, H. M. Line profiles of neutron powder–diffraction peaks for structure refinement. *Acta Crystallographica.* **22**, 151–152, doi:10.1107/S0365110X67000234 (1967).

45. Rietveld, H. M. A profile refinement method for nuclear and magnetic structures. *Journal of Applied Crystallography.* **2**, 65–71, doi:10.1107/S0021889869006558 (1969).

46. Cheary, R. W. & Coelho, A. A fundamental parameters approach to X–ray line–profile fitting. *Journal of Applied Crystallography.* **25**, 109–121, doi:10.6028/jres.002 (1992).

47. TOPAS v. 4.2 (Bruker AXS Inc., USA, 2009).

Acknowledgements

Author Contributions

Guangshi Li, Hongwei Cheng and Xionggang Lu conceived, designed and coordinated the study; Guangshi Li performed the experiments and processed the data; Hongwei Cheng, Xionggang Lu, Xingli Zou and Qian Xu contributed reagents/materials/analysis tools. Xiaolu Xiong, Cong Xu and Changyuan Lu contributed to the discussion of the results as well as to the writing of the manuscript.

Additional Information

Supplementary information accompanies this paper at doi:10.1038/s41598-017-03290-y

Competing Interests: The authors declare that they have no competing interests.

Publisher's note: Springer Nature remains neutral with regard to jurisdictional claims in published maps and institutional affiliations.